Journal of Power Sources 189 (2009) 179–184

Contents lists available at ScienceDirect

Journal of Power Sources

journal homepage: www.elsevier.com/locate/jpowsour

Nanosized high voltage cathode material $LiMg_{0.05}Ni_{0.45}Mn_{1.5}O_4$: Structural, electrochemical and in situ investigation

U. Lafont[a,*], C. Locati[a], W.J.H. Borghols[b], A. Łasińska[c], J. Dygas[c], A.V. Chadwick[d], E.M. Kelder[a]

[a] NanoStructured Materials, DCT/TUDelft, Julianalaan 136, 2628BL Delft, The Netherlands
[b] Fundamental Aspects of Materials and Energy, R3/TUDelft, Mekelweg 15, 2629JB Delft, The Netherlands
[c] Faculty of Physics, Warsaw University of Technology, Koszykowa 75, 00-662 Warszawa, Poland
[d] Functional Materials Group, School of Physical Sciences, University of Kent, Canterbury CT2 7NR, United Kingdom

ARTICLE INFO

Article history:
Received 25 July 2008
Received in revised form
25 September 2008
Accepted 26 September 2008
Available online 19 October 2008

Keywords:
High voltage spinel
In situ XANES
Li-ion battery
Nanomaterials
$LiNi_{0.5}Mn_{1.5}O_4$

ABSTRACT

In this study a modified solid state synthesis (auto-ignition method) is used to form nanosized spinel type material $LiMg_{0.05}Ni_{0.45}Mn_{1.5}O_4$. This material presents a high voltage plateau at 4.75 V vs. Li/Li^+. Structural and electrochemical characterisations have been performed using a wide range of techniques (TEM, neutron diffraction, galvanostatic measurements, and impedance spectroscopy). Besides, in situ XAS has been performed to monitor the evolution of Ni and Mn oxidation state during Li intercalation. The material presents an ordered cubic spinel structure, good capacity retention upon cycling (131 mAh g^{-1} at C/10 and 117 mAh g^{-1} at 1C) and good electronic conductivity (10^{-6} S cm^{-1} at RT). The simultaneous presence of Mn^{3+}/Mn^{4+} in the structure has been investigated and explained by inclusion of disordered nanodomains in the structure.

1. Introduction

Nowadays, many political decisions, supported by scientific research, concern the implementation of Li-ion batteries, because they are seen as key electrical storage media for a sustainable transition to non-polluting automotive vehicles (HEV, EV and PHEV). Most of the commercial Li-ion batteries are still used for portable electronics, and use typically a carbonaceous based material as negative electrode and a ~4-V transition metal oxide as positive electrode. For high power application, the use of carbonaceous based material and their derivatives with the PC-containing electrolytes in these systems are not safe enough to fulfil safety demands for commercial applications. Indeed, during the International Meeting on Li-ion Battery 2008, the safety issue of Li-ion batteries for automotive application was a "hot topic". In this respect, although it is known for several years, the $Li_4Ti_5O_{12}$ spinel (LTO) material present most of the requirements needed for commercial high power applications, i.e. safe, cheap, non-toxic, has excellent reversibility and structural stability (zero strain during Li insertion and removal). The main disadvantage of this material is the working voltage of 1.5 V vs. Li/Li^+. However, the 1.5 V plateau can avoid the carbonate based electrolyte solvent to decompose into gaseous products. Using LTO material as negative electrode will give a cell of 2.5 V using a state-of-the-art 4 V cathode material. In order to obtain a sufficiently higher operating voltage, so called high voltage cathode materials are needed. Since a decade, the substitution of Mn by other transition metal ions, such as by Me = Ni, Co, Fe, Cu, Cr in $LiMn_2O_4$ has been extensively studied [1–12] leading to a high voltage spinel $LiMe_{0.5}Mn_{1.5}O_4$ and $LiMeMnO_4$. In this respect, $LiNi_{0.5}Mn_{1.5}O_4$ and $LiCrMnO_4$ material are the only ones presenting a sufficiently well define high voltage plateau [13].

On the one hand it is clear that high voltage materials are needed and the $LiNi_{0.5}Mn_{1.5}O_4$ type material being the most promising system has been extensively studied. On the other hand, beside progress made on electrode engineering, nanosized material can be of great help due to an enhanced charge transfer surface area per weight and improved rate capability [14–16] due to a reduced diffusion/migration-length compared to state-of-the-art cathode materials sizes.

In this study we will focus on the structural and electrochemical characterisation of Mg and Ni substituted nanosized spinel material $LiMn_2O_4$ [14,15,17–19], $LiMg_{0.05}Ni_{0.45}Mn_{1.5}O_4$, exhibit-

* Corresponding author. Tel.: +31 152785536; fax: +31 152784945.
E-mail address: u.lafont@tudelft.nl (U. Lafont).

0378-7753/$ – see front matter © 2008 Elsevier B.V. All rights reserved.
doi:10.1016/j.jpowsour.2008.09.121

ing 148.10 mAh g^{-1} of theoretical capacity. The Mg atoms are not directly involved in redox reactions during lithium intercalation/deintercalation. As it has been demonstrated in previous work [17,18], Mg substitution lowers the polarization and enhances the overall insertion kinetics by increasing electronic conductivity [20] and will not be discuss in this paper. The increase in conductivity by Mg substitution has also been demonstrate in the $Li_{1-x}Mg_xTi_5O_{12}$ system [20].

2. Experimental

2.1. Synthesis

The synthesis route adopted during this study is called auto-ignition method. This method exploits the highly exothermic reactions that happen during the combustion of a fuel and an oxidizer to maintain a self-propagating reaction giving a high reaction temperature. The compound $LiMg_{0.05}Ni_{0.45}Mn_{1.5}O_4$ was synthesized by mixing metallic salts precursors $LiNO_3$, $Mg(NO_3)_2{\cdot}6H_2O$, $Ni(NO_3)_2{\cdot}6H_2O$ and $Mn(CH_3COO)_2{\cdot}4H_2O$ (Aldrich) with a certain amount of urea, that acts as the additional fuel. The molar composition then of the precursors Li:Mg:Ni:Mn:Urea is 0.05:0.0025:0.0225:0.075:4.5, respectively. The mixed precursors are thermally treated at 700 °C for 12 h under air (5 °C min^{-1} rate). The resulting material presents a brownish foamy powder texture. The as-synthesized powders were further crushed into a mortar.

2.2. Structure characterisation

The composition of the final product is analysed with the Inductively Coupled Plasma technique using a PerkinElmer Optima 5300. The surface area of the powders produced was measured via the BET method using nitrogen adsorption with a Quantachrome Autosorb-6B. Transmission electron microscopy (TEM) was performed using a Philips CM30T electron microscope with a LaB6 filament as electrons source operated at 300 kV. Neutron diffraction measurements were performed at POLARIS, the high intensity general-purpose time-of-flight powder diffractometer at the ISIS pulsed neutron source (Rutherford Appleton Laboratory, UK). The quasi in situ XANES measurements in the Mn K- and Ni K-edges were carried out on station 7.1 at the SRS at Daresbury (UK). The measurements were performed in normal transmission mode using gas-filled ion chambers. A third ion chamber was used to collect the XAS of a metal foil placed after the signal ion chamber. This provided a reference for the calibration of the edge position for each scan. The synchrotron energy is 2 GeV, and the average ring current during the experiments was 150 mA. The energy scales were calibrated taking as the zero the Mn K- and Ni K-edges of Mn (6538 eV) and Ni foils (8332 eV), respectively. For the quasi in situ measurements, "coffee bag" cells using the Bellcore technology [21] were assembled. The cells were stopped at a certain state charge–discharge during the measurement period.

2.3. Electrochemical characterisation

The electrochemical tests were performed using a Maccor S4000 in galvanostatic mode at room temperature. For this purpose, active material, polyvinylidene fluoride (Solvay), carbon black (>99.9%, <1.0 μm; Alfa) and graphite (≤0.1 mm; Fluka) (80:10:3:7 wt.%) were mixed with 1-methyl-2-pyrrolydon (NMP, Merck-Schuchardt). The resulting paste is ball-milled for 15 min and then deposited on an aluminum strip with a 200-μm thick doctor-blade and immediately dried at 80 °C for a couple of hours. The aluminium strip is then laminated until 70 μm thickness. The electrochemical tests were done in CR2320-type coin-cells (Hohsen), with a 14-mm electrode, polyethylene separator (Solupor), polypropylene gasket, LiPF6 1 mol l^{-1} in EC/DMC (2:1) (Mitsubishi Chemical), and a 16-mm Li disk, that is used as counter and reference electrode. The coin-cells were sealed in a He-filled glove box (O_2 < 1 ppm and H_2O < 5 ppm). The cells for impedance measurements were prepared in a glove box under argon atmosphere. Pressed pellets with gold electrodes were mounted between gold plated stainless steel electrodes in a gas tight holder. The holder was placed in a thermostat, heated or cooled by Peltier elements between −60 °C and 150 °C. Temperature was controlled by Eurotherm 2408. Impedance spectra were recorded at constant temperature during heating and cooling runs. A computer-controlled set-up based on a Solartron 1260 impedance analyser and a Keithley 428 current amplifier was used in the frequency range from 10^7 Hz down to 10^{-1} Hz. The amplitude of the ac signal was 30 mV rms.

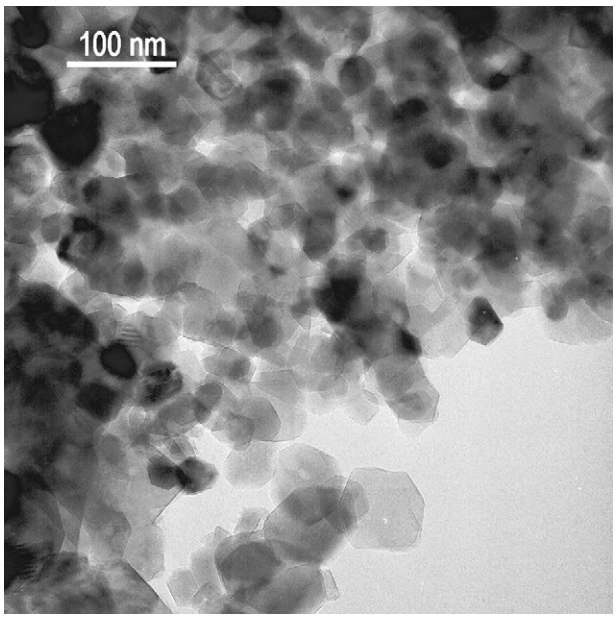

Fig. 1. TEM micrograph of $LiMg_{0.05}Ni_{0.45}Mn_{1.5}O_4$ synthesized by auto-ignition method.

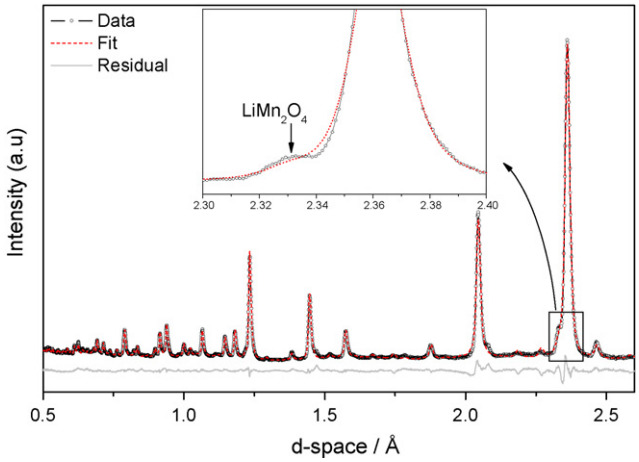

Fig. 2. Neutron diffraction data of $LiMg_{0.05}Ni_{0.45}Mn_{1.5}O_4$ showing the observed intensities (black line with open circles) and the refined one (red dotted line). The grey line represents the residual part. The insert shows the extra phase attributed to $LiMn_2O_4$ (*Fd*−3*m*). (For interpretation of the references to color in this figure legend, the reader is referred to the web version of the article.)

Table 1
Refined structural parameters for $LiMg_{0.05}Ni_{0.45}Mn_{1.5}O_4$.

Phase	Atom	Site	x/a	y/b	z/c	Fraction [0,1]
$P4_332$ cubic space group 212, a = 8.1748 Å, wRp = 0.049, Rp = 0.048	Li	8c	−0.001	0	0	0.81
	Li	4a	1/8	1/8	1/8	0.38
	Mg	4b	5/8	5/8	5/8	0.10
	Ni	4b	5/8	5/8	5/8	0.65
	Mn	4b	5/8	5/8	5/8	0.23
	Ni	12d	1/8	0.4173	0.8327	0.08
	Mn	12d	1/8	0.4007	0.8493	0.92
	O	8c	0.3884	0.3884	0.3884	1.00
	O	24e	0.1069	0.1214	0.3902	1.00

3. Results and discussion

3.1. Structure characterisation

The synthesized material by the auto-ignition method presents a final composition of $Li_{0.98}Mg_{0.049}Ni_{0.44}Mn_{1.55}O_4$ measured with ICP. The surface area deduced from the nitrogen adsorption isotherm using the BET theory is 4.5 $m^2\,g^{-1}$. The material does not present any structural porosity. Indeed, the TEM micrograph (Fig. 1) exhibits soft agglomerates of 20–80 nm particles. The particles reflect clearly the cubic structure of the spinel phase the material exhibits.

Fig. 2 displays the observed neutron diffraction pattern together with the refined spectrum calculated with the Rietveld method. Here the residual error is about 5% and the corresponding error curve is plotted as a grey line in Fig. 2. This error is mainly due to an extra phase in the material, which reflections are resolved by assuming a contamination of about 2% of $LiMn_2O_4$ (space group *Fd3m*) in the sample. The main reflection of this extra phase is present at 2.33 Å. It is, however, stressed that, a full confirmation cannot be given as the 2% calculated as contamination is within the accuracy limits of the refinements. Nevertheless, the peak near 2.33 Å is clearly visible by eye. Further from Rietveld refinement, the particle size was calculated to be 51 (±4) nm. The refinement data as the unit cell parameters and the atomic position are gathered in Table 1. Since the data were best refined according to the $P4_332$ space group, the $LiMg_{0.05}Ni_{0.45}Mn_{1.5}O_4$ adopts an ordered cubic spinel structure.

3.2. Electrochemical characterisation

Electrochemical impedance spectroscopy results of the pressed pellets are shown in Fig. 3. Impedance measurement are recorded as a function of temperature T, ranging from −60 to 200 °C. In order to calculate the Li-ion conductivity $\sigma(T)$, the recorded spectra – not shown here – are fitted to a state-of-the-art equivalent circuit. Typically, the material presents a conductivity of 10^{-6} S cm^{-1} at 25 °C. The activation energy E_a deduced from the data is calculated using an Arrhenius type dependency, i.e. $\sigma(T) = A\exp^{[-E_a/kT]}$, with A a pre-exponential factor and k the Boltzmann constant. The obtained E_a values are 0.37 eV in the temperature range −40 to 30 °C, 0.40 eV in temperature range 30–100 °C and 0.41 eV in temperature range 100–140 °C.

The galvanostatic charge–discharge measurements are plotted in Fig. 4. The experiments were performed using different successive current rates, ranging from 15 to 750 mA g^{-1} (giving a C-rate of C/10 to 5C), and finally back to 30 mA g^{-1} (C/5). Data were recorded for at least five charge–discharge cycles.

Irrespective of the current used, the curves present the same charge behaviour showing a high voltage plateau between 4.71 and 4.77 V. This plateau is attributed to the successive oxidation of Ni^{2+} to Ni^{3+} and Ni^{4+}. For currents from 15 to 150 mA g^{-1} (C/10 to C) all the charge curves present a plateau near 4.1 V. This plateau, however, disappears at higher charge current (300 and 750 mA g^{-1}, i.e. 2C and 5C, respectively). The de-intercalation of Li, i.e. taking out Li-ions from the spinel structure, at this voltage is attributed to the oxidation of Mn^{3+} to Mn^{4+}. For the discharge profile (Li intercalation) the high voltage plateau is shifted to lower voltages when the discharge current is increased.

From Fig. 5 we see that increasing the current rate during the charge and discharge lead to significant loss of capacity. It is remark-

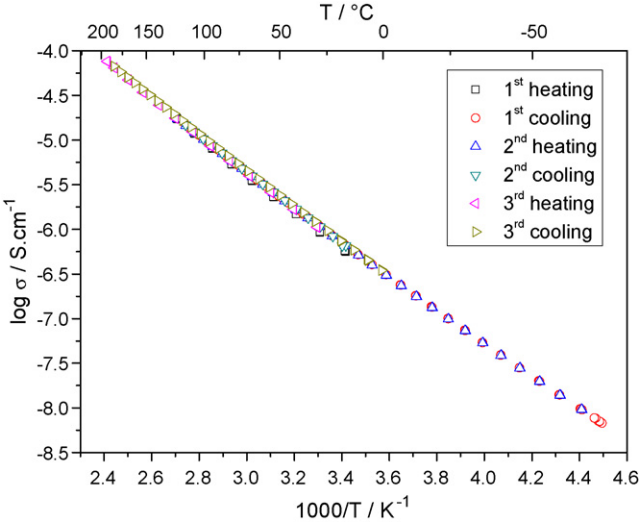

Fig. 3. Temperature dependency of the conductivity of $LiMg_{0.05}Ni_{0.45}Mn_{1.5}O_4$.

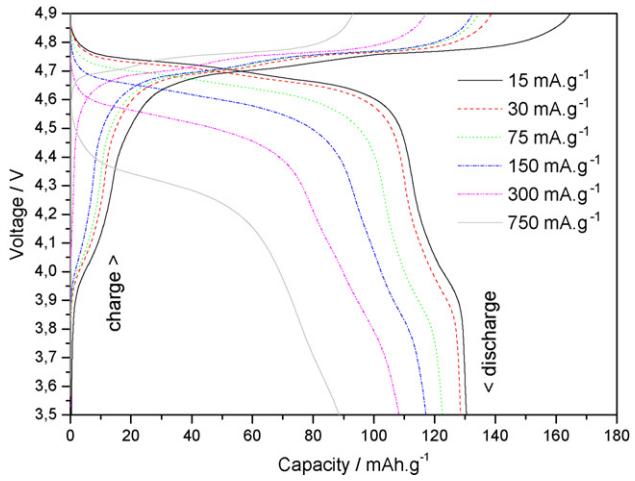

Fig. 4. Charge–discharge profile in galvanostatic mode at various C rate vs. Li/Li^+.

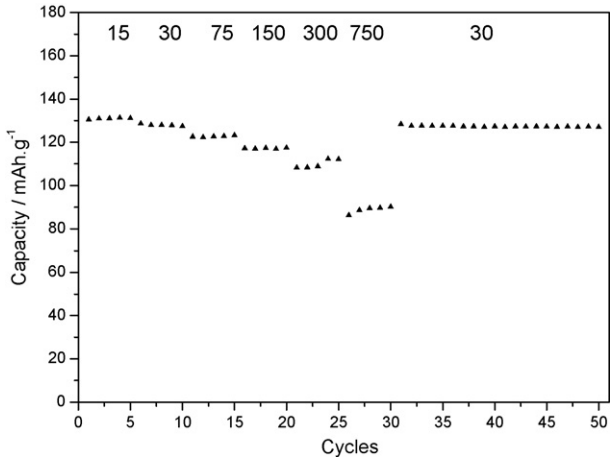

Fig. 5. Discharge capacity as a function of cycle number and C rate in mA g^{-1} (top).

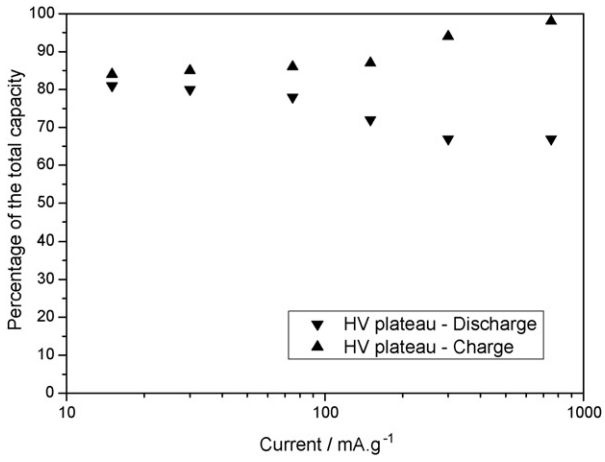

Fig. 6. Percentage of the total capacity attributed to the high voltage (HV) plateau as a function of the current rate.

able that irrespective of the charge current used, the capacity retention upon cycling is really stable within that specific current rate. The capacity measures at the various current rates are gathered in Table 2.

After the series of charging and discharging at various rates, the system was charged and discharged at a C/5 rate, i.e. 30 mA g^{-1}. The obtained capacity at the end stage is 128 mAh g^{-1}, showing complete recovering of the initial capacity. Further cycling of the cell does not show anymore degradation.

From the galvanostatic measurements it is clear that the origin of the capacity is not only due to the oxidation/reduction of Ni^{2+}/Ni^{4+} species at 4.75 V. The total capacity presents a non-negligible contribution coming from the oxidation/reduction of the Mn^{3+}/Mn^{4+} species near 4.1 V. In this respect, we plotted in Fig. 6, the percentage of the total capacity attributed to the oxidation/reduction of the Ni species (the high-voltage plateau at 4.75 V) during the charge and discharge at different current rates. During the charge, the percentage of this part increased from 84 to 98% upon increasing the current from 15 to 750 mA g^{-1}, respectively. During the discharge process, this value is decreasing from 81 to 60% with increasing the current. This phenomenon can be explained in terms of an alleged energy barrier. According to Ceder et al. [22], Li diffusion is faster when the metals of the host structure present a low oxidation state so as to minimise the lithium-metal repulsion. At high C-rate, during the charge, Li^+ transport will encounter much less repulsion and overcome a lower energy barrier on Ni^{2+}/Ni^{3+} transition than on Mn^{3+}/Mn^{4+}. Besides, the distribution of the Mn in the overall material may play a role as well, as will be explained later on.

3.3. *In situ structure analysis*

Fig. 7 shows the curves of the Ni K-edge (8332 eV) and the Mn K-edge (6538 eV) XANES spectra obtained at various voltages during charge and discharge recorded between 3.5 and 4.9 V. The curves for the Ni K-edge have been recorded during the first cycle (charge and discharge) whereas the curves for the Mn K-edge are recorded during the first cycle for the charge and during the second cycle for the discharge. The Ni K-edge is shifted to higher energy during the charge indicating a change in the oxidation state. The pristine material presents an average oxidation state of +2.6. Some Ni species

Table 2
Capacity obtained as a function of the current rate.

Current rate (mA g^{-1})	C-rate	Capacity (mAh g^{-1})
15	C/10	131
30	C/5	128
75	C/2	122
150	C	117
300	2C	108
750	5C	90

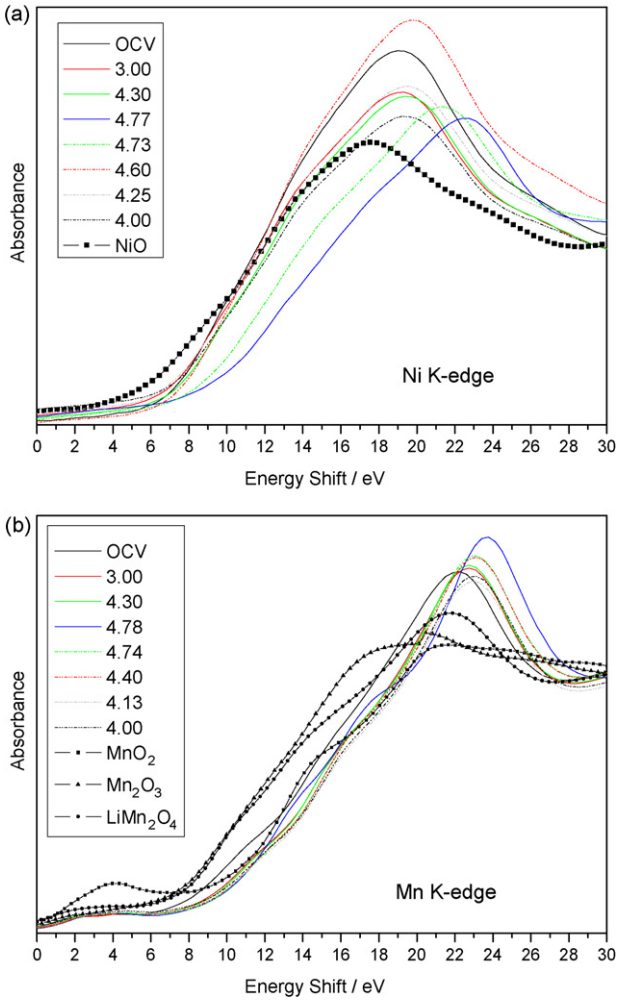

Fig. 7. In situ XANES spectra at different voltage during charge–discharge vs. Li/Li^+ at C/5 (a) Ni K-edge and (b) Mn K-edge.

present an initial oxidation state higher than the expected oxidation state of +2. At 4.9 V (end of charge) all Ni species present a +4 oxidation state. During the discharge, the Ni is reduced and at 4.5 V (end of the high-voltage plateau), all the Ni atoms present an average oxidation state of +2.7. It is stressed that the high voltage behaviour of this material is due to a reversible oxidation/reduction of Ni^{2+}/Ni^{4+}.

The shift, induced by a change in the Mn oxidation state, is less pronounced. Obviously, the pristine material of $LiMg_{0.05}Ni_{0.45}Mn_{1.5}O_4$ shows an initial Mn oxidation state of around +3.57. During the first charge the Mn atoms quickly adopt a maximal value of +4 at 4.78 V. During the discharge in the second cycle, the average oxidation sate is stable at +3.8 until 4 V. From this change in oxidation state, it is concluded that around 20% of the Mn atoms can be reversibly oxidized and reduced.

The $LiMg_{0.05}Ni_{0.45}Mn_{1.5}O_4$ material, synthesized by the auto-ignition method, exhibits a multi cation valency. Indeed, in the pristine material not all the Ni atoms show a +2 oxidation state and not all the Mn atoms have a +4 oxidation state as expected for pure ordered $LiMg_{0.05}Ni_{0.45}Mn_{1.5}O_4$. From electrochemical measurements and XANES investigations it is clear that the material present a certain amount of Mn^{3+} ions. The presence of these Mn^{3+} ions in the spinel structure implies a Jan-Teller distortion upon cycling, which is usually responsible of the degradation of the electrochemical properties of the material. However, some recent studies focussing on $LiNi_{0.5}Mn_{1.5}O_4$, $LiNi_{0.4}Mn_{1.6}O_4$ [23], $LiMn_{1.5+d}Ni_{0.5-d}O_4$ [16] and $LiMn_{2-x}Ni_xO_4$ [24] spinel materials describe the spinel in a disordered ($Fd{-}3m$) and an ordered ($P4_332$) cubic phase. During electrochemical tests vs. Li/Li^+ the disordered phase exhibits a plateau around 4–4.1 V whereas the ordered phase does not. Therefore, the disordered phase present Mn^{3+} ions in the structure, whereas in the ordered phase only Mn^{4+} and Ni^{2+} ions are present, and which they are ordered in 3:1 ratio on octahedral sites. From the electrochemical tests on this type of material performed so far [14–16,23–25], the positive effect of the presence of Mn^{3+} cations for high rate application is clear. The electronic conductivity is also influenced by cation ordering in the structure: the disordered phase can exhibit a 2.5 orders of magnitude higher conductivity [24] compared to the conductivity of the ordered phase, i.e. 10^{-7} S cm^{-1}. Our material had a conductivity of 10^{-6} S cm^{-1} that can be attributed to a beneficial effect of the Mg ions [17] and the nanosized particles as it has been reported earlier [14,15]. However the relation between the presence of Mn^{3+} and the pure disordered material is not clear yet. Obviously, our material presents all the electrochemical characteristics of a disordered cubic phase, i.e. the presence of a Mn^{3+}/Mn^{4+} oxidation reduction at 4–4.1 V, but reveals an ordered cubic structure ($P4_332$) from neutron diffraction data. As mentioned earlier, around 2% of $LiMn_2O_4$ was detected by neutron diffraction. This low amount of extra phase observed with neutron diffraction, partly contribute to the Mn^{3+} presence but cannot explain completely the significant amount of Mn^{3+}/Mn^{4+} oxidation and reduction seen during electrochemical experiments. To understand this disagreement and find out where the Mn^{3+} arises from, we propose two models:

- Mn^{3+} species are located at the outer part of the particles – the surface – and are responsible for the relaxation of the $LiMg_{0.05}Ni_{0.45}Mn_{1.5}O_4$ structure as formed during the synthesis.
- Mn ions exist in clusters within $LiMg_{0.05}Ni_{0.45}Mn_{1.5}O_4$ crystallites so as to create Mn rich and Mn poor domains in the particles.

The first model implies a serial insertion/extraction mechanism for ions and electrons in which the surface Mn ions have to react before the core Ni ions are being reached. In this case, irrespective of the C rate, the Mn^{3+}/Mn^{4+} transition should always been seen. Clearly, this does not happen in our system at high C rate. The second model is based on a parallel system in which some Mn rich nanodomains are present in the ordered $LiMg_{0.05}Ni_{0.45}Mn_{1.5}O_4$ particles. Indeed, this Mn rich domain will present Mn^{3+} ions like in a disordered cubic structure. The small size of these domains within one particle of ordered spinel cannot be detected by neutron diffraction but their presence can be suggested as it is shown in Fig. 8.

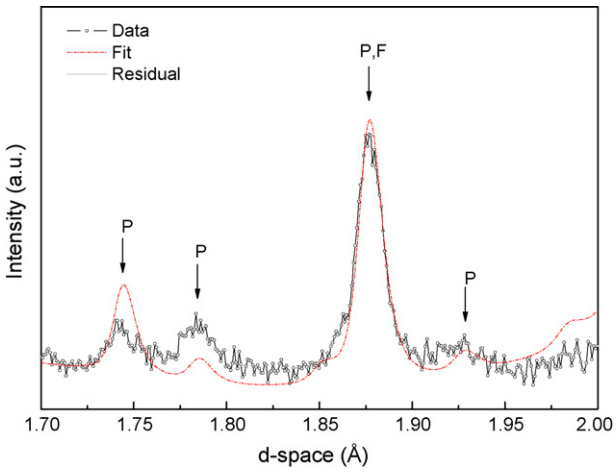

Fig. 8. Neutron diffraction of $LiMg_{0.05}Ni_{0.45}Mn_{1.5}O_4$. The reflections belonging to the $P4_332$ and $Fd{-}3m$ space groups are labelled as P and F, respectively.

Obviously, the neutron diffraction data show the main reflections of an ordered cubic phase ($P4_332$) that can clearly be distinguish from the disordered one ($Fd{-}3m$) [19]. However the fitting of the reflections at 1.745 and 1.785 Å show a difference in intensity and peak width, which can be attributed to either perturbations within the ordering or a shorter range ordering due to some local difference in cation ordering, hence Mn clusters.

4. Conclusion

With the synthesis process used in this research we were able to form $LiMg_{0.05}Ni_{0.45}Mn_{1.5}O_4$ nano-particles of ~50 nm in size, showing an ordered cubic spinel phase ($P4_332$). This high voltage material present good capacity retention of 131 mAh g^{-1} at C/10 and 90 mAh g^{-1} at 5C. The Mg doping eventually supported by the nanosize of the particles allow this material to exhibit a good Li-ion conductivity at room temperature (10^{-6} S cm^{-1}) and good stability upon cycling even at high C-rate. The presence of the oxidation/reduction of Mn^{3+} and Mn^{4+} is evident and can be explained by Mn rich nanodomains within the nanosized particles. Therefore, for high power applications, the material is an interesting positive electrode in Li-ion batteries using $Li_4Ti_5O_{12}$ as an anode.

Acknowledgments

The authors would like to thank the European Commission for funding the European Network of Excellence ALISTORE, and in particular M. Morcrette for helping in the coffee bag cells preparation, A. Blacklocks for helping in XAS data treatments and M. Wagemaker for fruitful discussions.

References

[1] C. Sigala, D. Guyomard, A. Verbaere, Y. Piffard, M. Tournoux, Solid State Ionics 81 (1995) 167–170.
[2] K. Amine, H. Tukamoto, H. Yasuda, Y. Fujita, J. Electrochem. Soc. 143 (1996) 1607–1613.

[3] Y. Gao, K. Myrtle, M. Zhang, J.N. Reimers, J.R. Dahn, Phys. Rev. B 54 (1996) 16670.
[4] K. Amine, H. Tukamoto, H. Yasuda, Y. Fujita, J. Power Sources 68 (1997) 604–608.
[5] Q.M. Zhong, A. Bonakdarpour, M.J. Zhang, Y. Gao, J.R. Dahn, J. Electrochem. Soc. 144 (1997) 205–213.
[6] Y. Ein-Eli, J.W.F. Howard, S.H. Lu, S. Mukerjee, J. McBreen, J.T. Vaughey, M.M. Thackeray, J. Electrochem. Soc. 145 (1998) 1238–1244.
[7] Y. Ein-Eli, S.H. Lu, M.A. Rzeznik, S. Mukerjee, X.Q. Yang, J. McBreen, J. Electrochem. Soc. 145 (1998) 3383–3386.
[8] H. Kawai, M. Nagata, M. Tabuchi, H. Tukamoto, A.R. West, Chem. Mater. 10 (1998) 3266–3268.
[9] H. Kawai, M. Nagata, H. Tukamoto, A.R. West, Electrochem. Solid State Lett. 1 (1998) 212–214.
[10] H. Kawai, M. Nagata, H. Tukamoto, A.R. West, J. Mater. Chem. 8 (1998) 837–839.
[11] Y. Ein-Eli, J.T. Vaughey, M.M. Thackeray, S. Mukerjee, X.Q. Yang, J. McBreen, J. Electrochem. Soc. 146 (1999) 908–913.
[12] H. Kawai, M. Nagata, H. Kageyama, H. Tukamoto, A.R. West, Electrochim. Acta 45 (1999) 315–327.
[13] H. Kawai, M. Nagata, H. Tukamoto, A.R. West, J. Power Sources 81 (1999) 67–72.
[14] U. Lafont, C. Locati, E.M. Kelder, Solid State Ionics 177 (2006) 3023–3029.
[15] C. Locati, U. Lafont, L. Simonin, F. Ooms, E.M. Kelder, J. Power Sources 174 (2007) 847–851.
[16] M. Kunduraci, G.G. Amatucci, Electrochim. Acta 53 (2008) 4193–4199.
[17] F.G.B. Ooms, E.M. Kelder, J. Schoonman, M. Wagemaker, F.M. Mulder, Solid State Ionics 152–153 (2002) 143–153.
[18] F.G.B. Ooms, M. Wagemaker, A.A.v. Well, F.M. Mulder, E.M. Kelder, J. Schoonman, Appl. Phys. A: Mater. Sci. Process. A74 (2002) S1089–S1091.
[19] M. Wagemaker, F.G.B. Ooms, E.M. Kelder, J. Schoonman, G.J. Kearley, F.M. Mulder, J. Am. Chem. Soc. 126 (2004) 13526–13533.
[20] C.H. Chen, J.T. Vaughey, A.N. Jansen, D.W. Dees, A.J. Kahaian, T. Goacher, M.M. Thackeray, J. Electrochem. Soc. 148 (2001) A102–A104.
[21] J.-M. Tarascon, A.S. Gozdz, C. Schmutz, F. Shokoohi, P.C. Warren, Solid State Ionics 86–88 (1996) 49–54.
[22] K. Kang, Y.S. Meng, J. Bréger, C.P. Grey, G. Ceder, Science 311 (2006) 977–980.
[23] S. Patoux, L. Sannier, H. Lignier, Y. Reynier, C. Bourbon, S. Jouanneau, F. Le Cras, S. Martinet, Electrochim. Acta 53 (2008) 4137–4145.
[24] M. Kunduraci, J.F. Al-Sharab, G.G. Amatucci, Chem. Mater. 18 (2006) 3585–3592.
[25] H.F. Xiang, Q.Y. Jin, R. Wang, C.H. Chen, X.W. Ge, J. Power Sources 179 (2008) 351–356.